

Aerodynamic Force Control for Tilt-Wing eVTOL Using Airflow Vector Estimation

Kentaro Yokota, *Student Member, IEEE*, and Hiroshi Fujimoto, *Senior Member, IEEE*

Abstract—Research and development are active in electric vertical takeoff and landing (eVTOL) aircraft. In particular, tilt-wing eVTOL aircraft receive much attention as one of the most efficient configurations; however, they are likely to be unstable during the transition from hover to cruise because the lift and thrust have limitations depending on the airflow and tilt angle. This study proposes a new aerodynamic force control method using airflow vector estimation. The airflow vector is estimated by combining motor current, rotational speed, and Pitot-tube measurements. Aerodynamic force control is achieved through the proper design of a feedback controller using disturbance observers to cope with propeller-wing interference caused by the propeller slipstream. This method takes advantage of the motor control performance and is unique in that it monitors the airflow vector and actively changes the tilt angle to quickly obtain the desired acceleration. The effectiveness of the method is verified via simulations and experiments in a wind tunnel.

Index Terms—Aircraft control, motion control, observers, parameter estimation, force control.

I. INTRODUCTION

A. Electric Flying Mobility

OWING to the increasing demand for personal and eco-friendly aviation, research and development in electric flying mobility (EFM), *e.g.*, in electric vertical takeoff and landing (eVTOL), have attracted attention. Given that EFM is powered by electric motors, it has the following advantages from a control engineering viewpoint:

- 1) The motor torque generation is 100 times faster than that of internal combustion engines [1].
- 2) The motor torque measurement is accurate [1].
- 3) Distributed installation (*i.e.*, DEP: distributed electric propulsion) and independent control of motors are easy [2].
- 4) Power regeneration is possible [3].

These advantages enable EFM to achieve more secure, efficient, and eco-friendly aviation.

The authors' research group has been studying new control methods for propeller-driven electric aircraft and proposed quick thrust and lift control methods [4], [5] as well as range extension systems [6] by adopting motion control theories developed in the automotive industry [7].

Manuscript received Month XX, 2021; revised Month XX, 2022. This work was partly supported by JSPS KAKENHI under Grant JP18H03768. (*Corresponding author: Kentaro Yokota.*)

Kentaro Yokota and Hiroshi Fujimoto are with the Department of Advanced Energy, Graduate School of Frontier Sciences, the University of Tokyo, Chiba, 277-8561, Japan. (e-mail: yokota.kentaro19@ae.k.u-tokyo.ac.jp; fujimoto@k.u-tokyo.ac.jp)

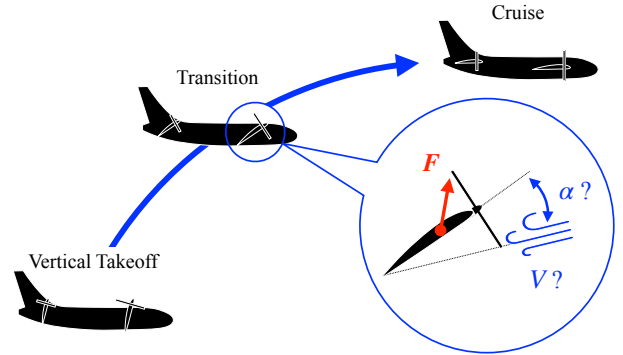


Fig. 1. Transition of tilt-wing aircraft.

B. eVTOL

Within the field of EFM, eVTOL is currently receiving much interest; eVTOL is expected to play a significant role in future urban air transportation. A few examples of passenger eVTOL under development are CityAirbus (Airbus), Vahana (Airbus), Ehang 216 (Ehang), Lilium Jet (Lilium), S-A1 (Uber Elevate), Bell Nexus 4EX (Bell), and SD-XX (SkyDrive). Most eVTOL aircraft can be categorized into four types: multi-copter, lift+cruise, tilt-rotor, and tilt-wing [8]. The differences in the configurations between these four categories are as follows. Multicopters have only upward thrusters. Lift+cruise aircraft have both upward and forward thrusters for hover and cruise, respectively. Tilt-rotor and tilt-wing use the same thrusters for hover and cruise by tilting actuators, allowing them to vertically takeoff and land like helicopters, and cruise like airplanes. Tilt-wing aircraft exhibit tilting wings with thrusters, and tilt-rotor aircraft have only tilting thrusters.

Compared to multicopters, fixed-wing eVTOL (*e.g.*, tilt-rotor and tilt-wing aircraft) enable high-speed and efficient cruise. In addition, tilt-rotor and tilt-wing aircraft require fewer actuators than lift+cruise aircraft. In particular, tilt-wing realizations present aerodynamic advantages over tilt-rotor ones because the propeller slipstreams are not disturbed by the tilting wings [9].

C. Transition of Tilt-Wing eVTOL

One of the most significant difficulties in the flight of tilt-wing aircraft is the transition from hover to cruise, as shown in Fig. 1. Given that the aerodynamic characteristics of the tilting wings and thrusters are complex, and tilt-wing aircraft in the transition state are similar to neither helicopters nor airplanes, they are likely to be unstable. Several studies were conducted on this problem [10], [11], [12], [13], [14], [15].

NASA investigated the limitations of tilt angle and airspeed using experimental UAV GL-10 [10], [11], [12] and LA-8 [13]. In addition, JAXA proposed a gain-scheduled control method for a quad tilt-wing UAV AKITSU [14], where the tilt angle was discretely altered to implement change in the aerodynamic characteristics.

D. Airflow Vector Estimation

The airflow vector, defined by the airspeed and angle of attack (AoA) as shown in Fig. 1, is a critical parameter for aircraft motion. For instance, the lift is determined by the airflow vector. Therefore, with real-time data of the airflow vector, tilt-wing aircraft would achieve a more robust transition.

There are a few methods for obtaining the AoA. One such method is airflow measurement [16]. However, it requires additional sensors that are usually non-standard equipment for personal aircraft. Another method is a model-based estimation. Many estimation methods have been proposed [17], [18], [19], [20], [21]; however, most of them are based on attitude and velocity measurements as well as aircraft models, and are not robust to propeller slipstreams, which are difficult to model. This problem becomes non-negligible with DEP, which takes advantage of the slipstreams for motion control. Therefore, they cannot be applied to tilt-wing aircraft, and a new AoA estimation method is necessary for a stable transition.

E. Aerodynamic Force Control

Feedback control in the acceleration dimension, such as control of force [4], [5] and acceleration [22], is often studied to improve aircraft stability. These methods make the most of the quick response of electric actuators and are also effective for tilt-wing transition. However, the lift and thrust of tilt-wing aircraft have limitations, which vary with the tilt angle, airspeed, and AoA. This limitation is a serious issue during the transition, leading to instability. Therefore, monitoring the airflow vector is indispensable for aerodynamic force control of tilt-wing aircraft. In addition, the tilt angle should not be considered as a change in the aerodynamic characteristics and should be used actively in the controller.

F. About This Study

This study aims to realize a new aerodynamic force control method using airflow vector estimation by taking advantage of motor control performance, in particular torque measurement from the motor current and quick torque responses. Accurate airflow vector estimation and fast aerodynamic force control cannot be achieved without these motor characteristics. However, previous studies did not focus on motor control. Thus, the contributions of this study can be summarized as follows:

- Airflow vector estimation from the motor current without requiring additional sensors
- Tilting algorithm for a stable transition in which the tilt angle is altered continuously
- Fast aerodynamic force control using the quick response of the motor

TABLE I
PARAMETER DEFINITIONS

| Symbol | Description | Unit | Definition |
|--------------------------------------|---|-------------------------|------------|
| α | Angle of attack (AoA) | rad, deg | Fig. 3 |
| δ | Flap angle | rad, deg | Fig. 3 |
| ρ | Air density | kg m^{-3} | |
| σ | Tilt angle | rad, deg | Fig. 3 |
| τ_δ | Time constant of δ controller | s | (40) |
| τ_n | Time constant of n controller | s | (39) |
| ϕ | Resultant flow angle | rad, deg | Fig. 2 |
| a_{bx}, a_{bz} | Acceleration along body axis | m s^{-2} | (37), (38) |
| a_p, b_p | Constants of s_p | – | (22) |
| $a_{\text{Pitot}}, b_{\text{Pitot}}$ | Constants of s_{Pitot} | – | (24) |
| B | Number of blades | – | Fig. 2 |
| B_ω | Viscosity coefficient of motor | N m s rad^{-1} | (13) |
| c | Chord of blade element | m | Fig. 2 |
| C_D | Drag coefficient | – | |
| C_F | Thrust coefficient of propeller | – | (7) |
| C_L | Lift coefficient | – | |
| C_Q | Torque coefficient of propeller | – | (8) |
| D_{bx}, D_{bz} | Drag and weight along body axis | N | (37), (38) |
| D_p | Propeller diameter | m | Fig. 2 |
| F | Propeller thrust | N | (11) |
| $F_{\sigma_x}, F_{\sigma_z}$ | Force along tilt axis | N | Fig. 3 |
| F_{bx}, F_{bz} | Force along body axis | N | Fig. 3 |
| J | Advance ratio | – | (10) |
| J_ω | Inertia moment of propeller | kg m^2 | (13) |
| K_δ | Slope of δ - F_{σ_z} relationship | N deg^{-1} | Fig. 10(c) |
| K_n | Slope of n - F_{σ_x} relationship | N rps^{-1} | Fig. 10(b) |
| m | Mass of aircraft | kg | |
| n | Rotational speed of propeller | rps | Fig. 2 |
| q | Dynamic pressure | Pa | (20) |
| Q | Counter torque of propeller | N m | (12) |
| S | Wing area | m^2 | |
| s_p | Angular sensitivity of propeller | – | (14) |
| s_{Pitot} | Angular sensitivity of Pitot tube | – | (23) |
| T | Input torque of motor | N m | (13) |
| T_C | Coulomb friction of motor | N m | (13) |
| V | Airspeed | m s^{-1} | Fig. 3 |
| V_p | Propeller airspeed | m s^{-1} | (15) |
| V_{Pitot} | Pitot-tube measurement | m s^{-1} | Fig. 3 |
| W | Resultant flow of blade element | m s^{-1} | Fig. 2 |

The remainder of this paper is organized as follows. Section II describes the modeling of tilt-wing aircraft. The airflow vector estimation method is described in Section III. Section IV describes the aerodynamic-force control method. Finally, Section V presents simulation and experimental results.

The definitions of the parameters used in this paper are shown in Table I.

II. MODELING

In this section, tilt-wing aircraft are modeled with a particular focus on propeller and wing dynamics.

A. Propeller

Fig. 2 shows velocities and forces acting on the propeller blade element when $\alpha = 0$. The blade element is r away from the center and has a thickness of dr ; dL is the differential lift and dD is the differential drag. The contribution of the blade element to F and Q is

$$dF = dL \cos \phi - dD \sin \phi, \quad (1)$$

$$dQ/r = dL \sin \phi + dD \cos \phi. \quad (2)$$

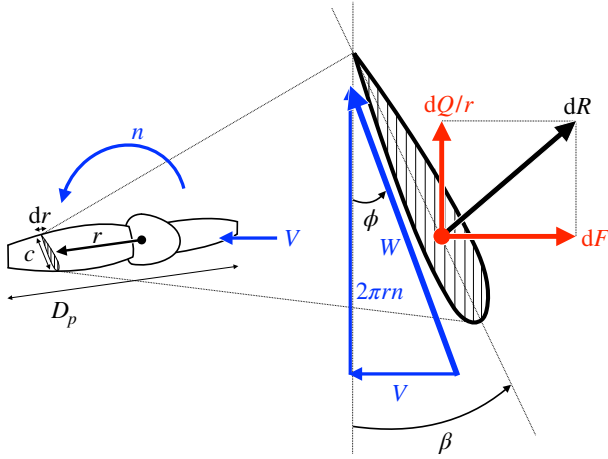


Fig. 2. Velocities and forces acting on propeller blade element (during cruise, $\alpha = 0$ in Fig. 3).

dL and dD can be calculated as

$$dL = \frac{1}{2} \rho W^2 c dr C_L, \quad (3)$$

$$dD = \frac{1}{2} \rho W^2 c dr C_D, \quad (4)$$

where c denotes the chord, C_L denotes the lift coefficient, and C_D denotes the drag coefficient. Let B be the number of blades. Then,

$$F = B \int dF = B \int (dL \cos \phi - dD \sin \phi), \quad (5)$$

$$Q = B \int dQ = B \int r (dL \sin \phi + dD \cos \phi). \quad (6)$$

Considering the theoretical equations (3)–(6), C_F and C_Q are defined according to experimental results as follows:

$$C_F = \frac{F}{\rho n^2 D_p^4}, \quad (7)$$

$$C_Q = \frac{Q}{\rho n^2 D_p^5}. \quad (8)$$

From Fig. 2, the angle of the resultant flow ϕ is determined by the ratio of V to $2\pi nr$.

$$\tan \phi = \frac{V}{2\pi nr} = \frac{J}{\pi \frac{2r}{D_p}}, \quad (9)$$

where J is defined by

$$J = \frac{V}{n D_p}. \quad (10)$$

Thus, C_F and C_Q are functions of J ; F and Q can be expressed as follows:

$$F = C_F(J) \rho n^2 D_p^4, \quad (11)$$

$$Q = C_Q(J) \rho n^2 D_p^5. \quad (12)$$

The equation of motion of the electric motor is

$$T - Q = 2\pi J_\omega \frac{dn}{dt} + 2\pi B_\omega n + T_C. \quad (13)$$

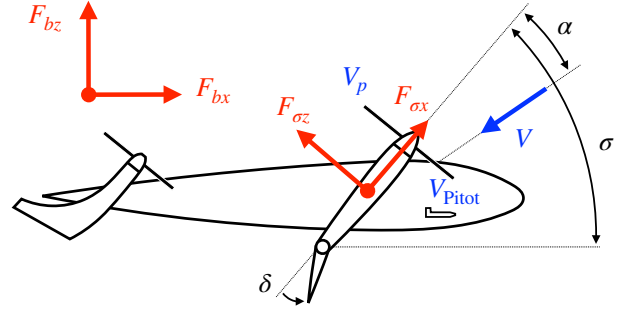


Fig. 3. Velocities and forces acting on wing and propeller (during transition, $\alpha \neq 0$).

B. Tilt-Wing

As shown in (11) and (12), C_F and C_Q are functions of $J = \frac{V}{n D_p}$ when $\alpha = 0$. However, when $\alpha \neq 0$, C_F and C_Q become functions of J and α . Let $s_p(\alpha)$ be the angular sensitivity of the propeller to airspeed. It is experimentally shown that C_F and C_Q become functions of J_p , defined by

$$J_p = J s_p(\alpha) = \frac{V_p}{n D_p}, \quad (14)$$

where V_p is the propeller airspeed defined by

$$V_p = V s_p(\alpha). \quad (15)$$

Thus, F and Q can be expressed as

$$F = C_F(J_p) \rho n^2 D_p^4, \quad (16)$$

$$Q = C_Q(J_p) \rho n^2 D_p^5. \quad (17)$$

The forces acting on the wing and propeller, *i.e.*, F_{σ_x} and F_{σ_z} , are defined by the propeller thrust, wing lift, and wing drag. The propeller thrust is determined by α , J , and V , as described above, and the wing lift and drag are determined by α , V , flap angle δ , and propeller slipstream. The propeller slipstream is determined by α , J , and V , and can be estimated by the Glauert's hypothesis [23]. This interaction between the propeller and wing makes the system complex and difficult to control.

Let $C_{F_{\sigma_x}}$ and $C_{F_{\sigma_z}}$ be the coefficients, which are functions of α , J , and δ . Thus, F_{σ_x} and F_{σ_z} can be expressed as

$$F_{\sigma_x} = C_{F_{\sigma_x}}(\alpha, J, \delta) q S, \quad (18)$$

$$F_{\sigma_z} = C_{F_{\sigma_z}}(\alpha, J, \delta) q S, \quad (19)$$

where the dynamic pressure q is expressed as

$$q = \frac{1}{2} \rho V^2. \quad (20)$$

III. PROPOSAL OF OBSERVER-BASED AIRFLOW VECTOR ESTIMATION

In this section, an observer-based airflow vector estimation method is proposed. This method estimates both the airflow angle and magnitude (α and V , respectively). Given that there are two estimation parameters, two sensors are required: the Pitot tube and motor torque. This method is based on propeller dynamics; therefore, a more direct estimation is achieved than with conventional estimation methods using inertial measurement units.

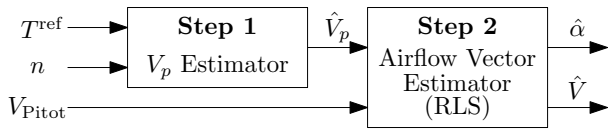


Fig. 4. Airflow vector estimator.

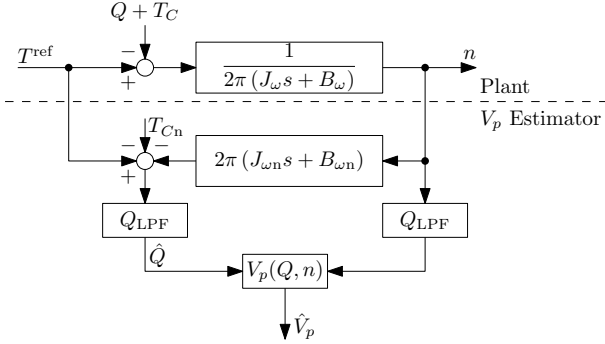


Fig. 5. Step 1: Propeller airspeed estimator.

The proposed method comprises two steps. Step 1 is the observer-based propeller airspeed estimation and Step 2 is the AoA estimation using the recursive least-squares (RLS) method. The overall estimation flow is shown in Fig. 4. The proposed method is based on the idea that the AoA can be calculated by the vector summation of V_p and V_{Pitot} ; however, the propeller and Pitot tube have their own angular sensitivity. Thus, these sensitivities must be modelled using wind-tunnel tests. This estimation method is based on a previous study of ours [24].

A. Step 1: Propeller Airspeed Estimation

For Step 1, the observer-based V_p estimation method is proposed. A block diagram of the V_p estimator is shown in Fig. 5. Because the motor torque can be accurately estimated from the motor current, V_p can be estimated from the motor current and the propeller model. The concept of airspeed estimation using motor torque was proposed in [25] and adopted in the observer-based estimation scheme in [26].

From (13), Q can be estimated by using a disturbance observer [27], [28], as shown in Fig. 5. $C_Q(J_p)$ typically has an inverse function in the operating region. Using (14), (17), and the estimated value of Q , V_p can be estimated as follows:

$$\hat{V}_p = n D_p C_Q^{-1} \left(\frac{\hat{Q}}{\rho n^2 D_p^5} \right). \quad (21)$$

Regarding the angular sensitivity of the propeller $s_p(\alpha)$, the wind-tunnel test results are shown in Fig. 6; $s_p(\alpha)$ is fitted by

$$s_p(\alpha) = a_p \cos \alpha + b_p \sin \alpha, \quad (22)$$

where a_p and b_p are constant.

B. Step 2: Airflow Vector Estimation

Using Step 1 and V_{Pitot} from the Pitot tube, the airflow vector is estimated in Step 2. To achieve airflow vector estimation,

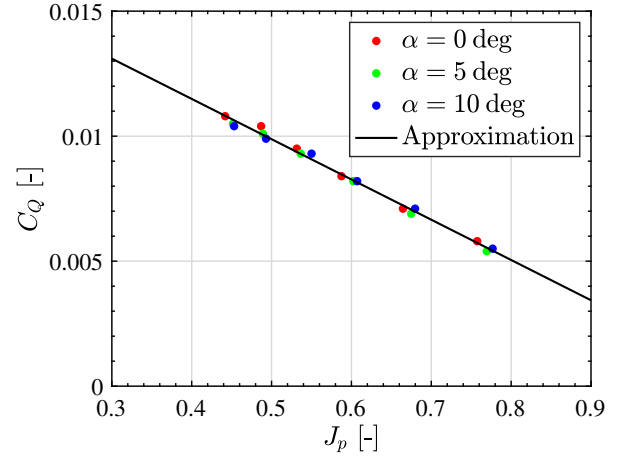
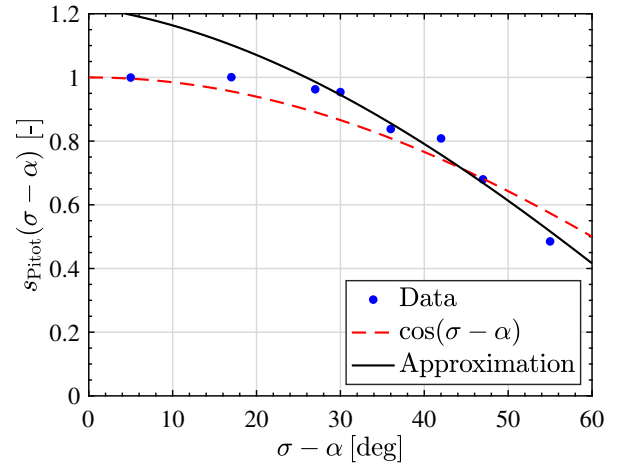
Fig. 6. Relationship between J_p and C_Q .

Fig. 7. Pitot tube's sensor characteristic.

the Pitot tube's sensor characteristic must be considered when $\sigma - \alpha \neq 0$. Let s_{Pitot} be the angular sensitivity of the Pitot tube, *i.e.*,

$$s_{\text{Pitot}}(\sigma - \alpha) = \frac{V_{\text{Pitot}}}{V}. \quad (23)$$

The relationship between $\sigma - \alpha$ and s_{Pitot} for the test Pitot tube is shown in Fig. 7. Note in this figure that s_{Pitot} is not equal to $\cos(\sigma - \alpha)$.

There are several functions for fitting this curve, such as a quadratic function. In this study, both $\cos(\sigma - \alpha)$ and $\sin(\sigma - \alpha)$ were used for simplicity. Thus,

$$s_{\text{Pitot}}(\sigma - \alpha) = a_{\text{Pitot}} \cos(\sigma - \alpha) + b_{\text{Pitot}} \sin(\sigma - \alpha), \quad (24)$$

where a_{Pitot} and b_{Pitot} are constant; a_{Pitot} and b_{Pitot} are determined using the least-squares method for the data above 20 deg. Given that only trigonometric functions are used for the AoA, this approximation simplifies the estimation equation (27).

From (15), (22), (24), and Step 1,

$$\hat{V}_p = V(a_p \cos \alpha + b_p \sin \alpha), \quad (25)$$

$$V_{\text{Pitot}} = V\{a_{\text{Pitot}} \cos(\sigma - \alpha) + b_{\text{Pitot}} \sin(\sigma - \alpha)\}. \quad (26)$$

Thus,

$$\begin{aligned} & -V_p (a_{\text{Pitot}} \cos \sigma + b_{\text{Pitot}} \sin \sigma) + V_{\text{Pitot}} a_p \\ & = \left\{ V_p (a_{\text{Pitot}} \sin \sigma - b_{\text{Pitot}} \cos \sigma) - V_{\text{Pitot}} b_p \right\} \tan \alpha. \end{aligned} \quad (27)$$

According to (27), the estimation equation becomes a function of only $\tan \alpha$. Note that σ is a measurable parameter.

Step 2 uses the RLS with a forgetting factor for noise reduction. In this estimation, the regression model is

$$y = \varphi \theta, \quad (28)$$

where the output y , regressor φ , and estimation parameter θ are expressed as follows:

$$y = -G_{\text{RLS}}(s) V_p (a_{\text{Pitot}} \cos \sigma + b_{\text{Pitot}} \sin \sigma) + V_{\text{Pitot}} a_p, \quad (29)$$

$$\varphi = G_{\text{RLS}}(s) V_p (a_{\text{Pitot}} \sin \sigma - b_{\text{Pitot}} \cos \sigma) - V_{\text{Pitot}} b_p, \quad (30)$$

$$\theta = \tan \alpha. \quad (31)$$

$G_{\text{RLS}}(s)$ is designed to align the phases of \hat{V}_p and V_{Pitot} based on the fact that the response of the Pitot tube is theoretically modeled as a first-order delay [29]. Updates of these parameters are calculated as follows:

$$\hat{\theta}[k] = \hat{\theta}[k-1] + \frac{P[k-1]\varphi[k]}{\lambda + P[k-1]\varphi^2[k]} \varepsilon[k], \quad (32)$$

$$\varepsilon[k] = y[k] - \varphi[k]\hat{\theta}[k-1], \quad (33)$$

$$P[k] = \frac{1}{\lambda} \left\{ P[k-1] - \frac{P^2[k-1]\varphi^2[k]}{\lambda + P[k-1]\varphi^2[k]} \right\}. \quad (34)$$

Finally, the estimated value of the AoA $\hat{\alpha}[k]$ can be calculated by

$$\hat{\alpha}[k] = \arctan \hat{\theta}[k]. \quad (35)$$

The airflow magnitude V can be estimated by

$$\hat{V}[k] = V_{\text{Pitot}}[k] \{ a_{\text{Pitot}} \cos(\sigma - \hat{\alpha}[k]) + b_{\text{Pitot}} \sin(\sigma - \hat{\alpha}[k]) \}. \quad (36)$$

IV. PROPOSAL OF AERODYNAMIC FORCE CONTROL

In this section, an aerodynamic force control method is proposed. As mentioned earlier, feedback control in the acceleration dimension improves aircraft stability. However, F_{σ_x} and F_{σ_z} have limitations depending on α and V , leading to acceleration limitations. Let a_{bx} and a_{bz} be the accelerations along the body axis, and let a_{bx} and a_{bz} be calculated by

$$a_{bx} = \frac{1}{m} (F_{bx} - D_{bx}), \quad (37)$$

$$a_{bz} = \frac{1}{m} (F_{bz} - D_{bz}), \quad (38)$$

where m is the mass of the aircraft and D_{bx} and D_{bz} are the aircraft weight and drag on the fuselage along the body axis, respectively. An example of the relationship between α , V and a_{bx} , a_{bz} is shown in Fig. 8. The circle around $a_{bx} = a_{bz} = 0$ is called the steady area, and the achievable a_{bx} and a_{bz} must include this area to maintain steady flight. If the aircraft were flying at α_1 and V_2 (red area) and the airspeed were increased to V_1 by a gust (green area), $a_{bx} = a_{bz} = 0$ could not be achieved. Therefore, the tilt angle σ must be decreased so

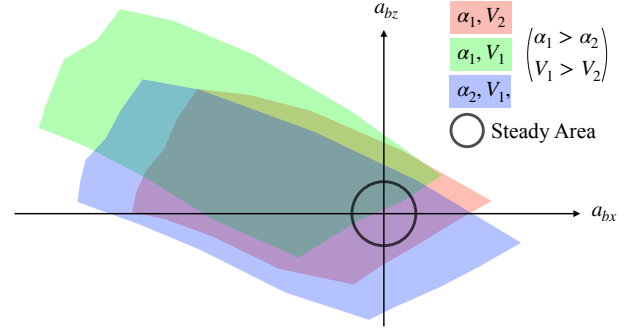


Fig. 8. Relationship between α , V and a_{bx} , a_{bz} .

that the AoA is changed to α_2 (blue area) to include the steady area.

With an achievable acceleration area including a steady area, the transition can be realized by accelerating in the direction of decreasing σ . Many studies have been conducted on path planning [14], [30]; therefore, this study focuses on aerodynamic force control to achieve the desired acceleration.

A. Controller Overview

An overview of the aerodynamic force controller is shown in Fig. 9. The force references F_{bx}^{ref} and F_{bz}^{ref} are converted into $F_{\sigma_x}^{\text{ref}}$ and $F_{\sigma_z}^{\text{ref}}$, respectively, by the rotation matrix $\mathbf{R}(\sigma)$. The force reference and feedback can be substituted by acceleration because most aircraft do not have force sensors.

$C_{\sigma FF}$ provides the tilt angle command, which can be obtained from the estimated airflow $\hat{\alpha}$, \hat{V} and the force references based on the algorithm explained above.

B. Controller Design

In the aerodynamic force controller shown in Fig. 9, F_{σ_x} is controlled by the propeller rotational speed n , and F_{σ_z} is controlled by the flap angle δ . Note that F_{σ_x} and F_{σ_z} interfere with each other owing to the propeller slipstream; however, this interference is assumed to be a disturbance and compensated by the feedback control.

The relationship between n , δ , α , V , and F_{bx} , F_{bz} in the experimental model that will be described later on is shown in Fig. 10. Note from Fig. 10(b) and Fig. 10(c) that F_{σ_x} and F_{σ_z} increase with n and δ , respectively.

Let K_n and K_δ be the slopes of the approximated line in Fig. 10(b) and Fig. 10(c). The nominal plant is given by the following expressions:

$$P_{\sigma_{xn}}(s) = \frac{F_{\sigma_x}}{n^{\text{ref}}} = \frac{K_n(V)}{\tau_n s + 1}, \quad (39)$$

$$P_{\sigma_{zn}}(s) = \frac{F_{\sigma_z}}{\delta^{\text{ref}}} = \frac{K_\delta(V)}{\tau_\delta s + 1}, \quad (40)$$

where τ_n is the time constant of the propeller rotational speed controller and τ_δ is the time constant of the flap angle controller. Note that K_n and K_δ are the functions of V . Hence,

$$n^{\text{ref}} = P_{\sigma_{xn}}^{-1}(s) F_{\sigma_x} + d_{\sigma_x}, \quad (41)$$

$$\delta^{\text{ref}} = P_{\sigma_{zn}}^{-1}(s) F_{\sigma_z} + d_{\sigma_z}. \quad (42)$$

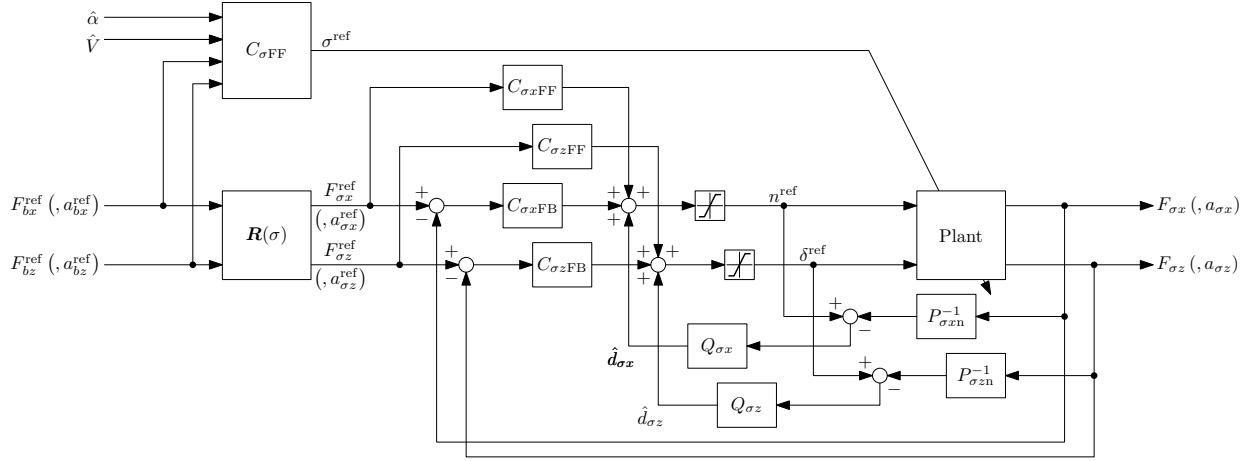


Fig. 9. Overview of aerodynamic force controller.

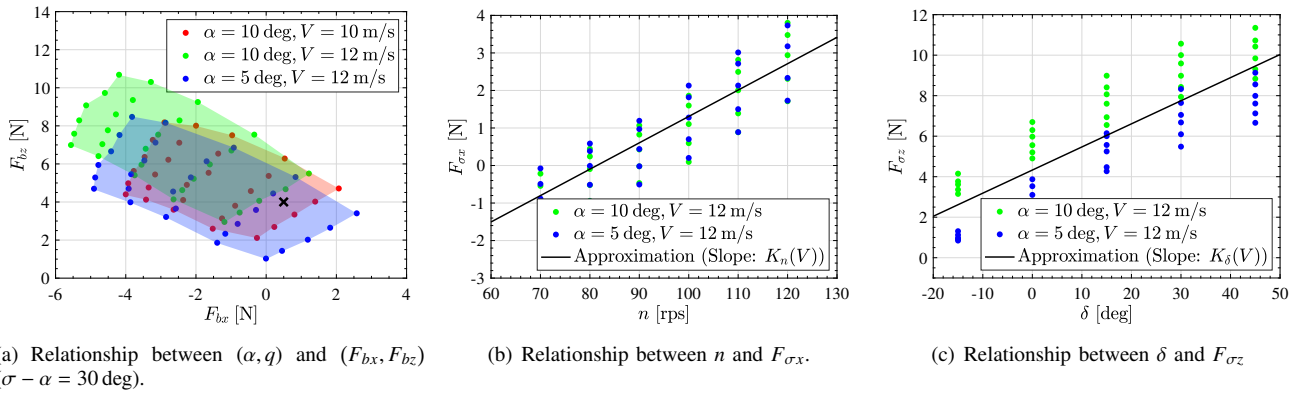


Fig. 10. Wind-tunnel test results in experimental model.

The feedback controller of each axis uses a disturbance observer (DOB). The DOB estimates and compensates the disturbances d_{σ_x} and d_{σ_z} . Note that d_{σ_x} and d_{σ_z} include the interference caused by propeller slipstream. Note also that Q_{σ_x} and Q_{σ_z} are first-order low-pass filters. The estimated disturbances \hat{d}_{σ_x} and \hat{d}_{σ_z} include the modeling error; therefore, the plant is normalized to $P_{\sigma_x n}$ and $P_{\sigma_z n}$ [27]. $C_{\sigma_x FB}$ and $C_{\sigma_z FB}$ are proportional controllers, and $C_{\sigma_x FF}$ and $C_{\sigma_z FF}$ are expressed as follows:

$$C_{\sigma_x FF} = \frac{1}{K_n(V)}, \quad (43)$$

$$C_{\sigma_z FF} = \frac{1}{K_\delta(V)}. \quad (44)$$

V. EXPERIMENTS AND SIMULATIONS

In this section, the wind tunnel experiments are described. The effectiveness of the proposed method is also discussed using additional simulations of aircraft motion based on the experimental results.

Fig. 11(a) shows a picture of the experimental setup. The experimental unit consisted of a Pitot tube, a tiltable wing with an APC 9 × 6 E propeller, and a six-component load cell on the stepping motor stage. The Pitot tube was tilted to simulate the propeller wing during transition, as shown in Fig. 11(b). Note that α can be altered by the stepping motor stage; its

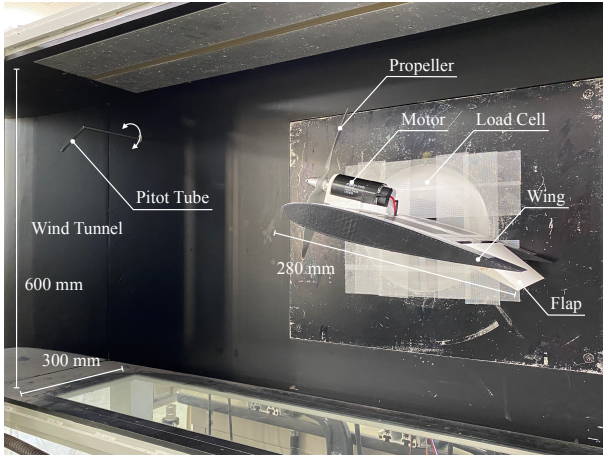
true value can be obtained from this stage. The true value of V was obtained by pre-experiments where the Pitot tube was not tilted, and the rotational speed of the wind-tunnel fan was set as in the main experiment. To maintain the accuracy of the wind-tunnel experiments, α was limited for the frontal height of the model not to exceed 1/10 of the height of the wind tunnel. Note that the wingspan only affects the force map shown in Fig. 10(a); it does not influence the estimation or controller design scheme.

A. Experimental Results of Airflow Vector Estimation

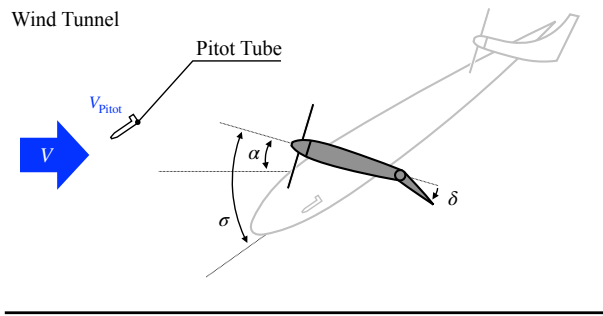
Fig. 12 shows the wind-tunnel test results of airflow vector estimation. In these experiments, α was set to 10 deg, V was set to 10 m s⁻¹, and $\sigma - \alpha$ was set to 30 deg. The sampling period was 1 ms. Note also that $\hat{\alpha}$ without RLS expresses the result of solving (27) for each sample. The estimation using RLS started at 0.01 s. Moreover, λ was set to 0.995, $\theta[0]$ was set to 0.178, and $P[0]$ was set to 10,000. Note from Fig. 12 that the airflow vector estimation provided an accurate estimation of α and V with little noise using RLS.

B. Experimental Results of Aerodynamic Force Control

Fig. 13 shows the wind-tunnel test results of aerodynamic force control. The poles of the F_{σ_x} and F_{σ_z} controllers were



(a) Picture of experimental setup.



(b) Correspondence between Fig. 3 and Fig. 11(a).

Fig. 11. Experimental setup.

placed at 5 rad s^{-1} . The initial α was set to 10 deg, the initial V was set to 10 m s^{-1} , and $\sigma - \alpha$ was set to 30 deg. The rotational speed of the wind-tunnel fan was changed stepwise at $t = 5 \text{ s}$ to reach $V = 12.5 \text{ m s}^{-1}$, as shown in Fig. 13(c). Fig. 13(b) and Fig. 13(c) show that the airflow vector was accurately estimated during the dynamic change in the airflow. F_{bx}^{ref} was 0.5 N , and F_{bz}^{ref} was 4 N . In the conventional method, airflow vector estimation was not employed and the same tilt angle σ was kept. Meanwhile, in the proposed method, airflow vector estimation was used and σ was flexibly changed to achieve the desired force, as shown in Fig. 13(a).

The black \times mark in Fig. 10(a) represents the force reference $(F_{bx}, F_{bz}) = (0.5, 4)$. Both the conventional and proposed methods started in the red area in Fig. 10(a), which includes the \times mark. As the airspeed increased, the achievable area shifted to the green area, which did not include the \times mark. Thus, the conventional method had error in F_{bx} and F_{bz} , as shown in Fig. 13(d) and Fig. 13(e). However, the proposed method accurately monitored the airspeed, as shown in Fig. 13(c), and shifted to the blue area in Fig. 10(a) by changing σ , as shown in Fig. 13(a). Therefore, F_{bx} and F_{bz} did not have errors in the proposed method.

C. Simulation Results of Aircraft Motion

To evaluate the effectiveness of the proposed method, a simulation of aircraft motion based on wind-tunnel tests of the propeller-wing model was conducted. The simulation param-

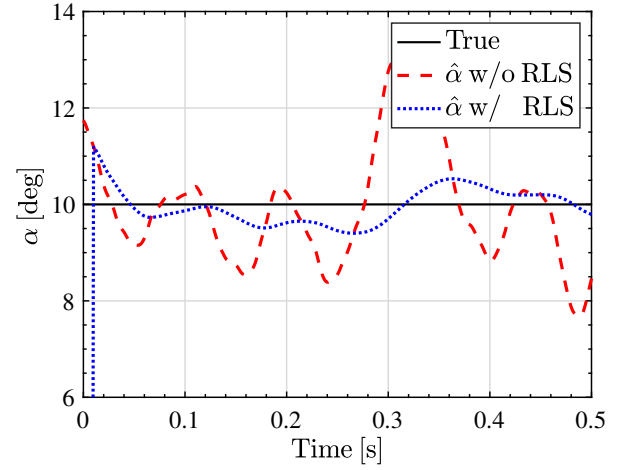
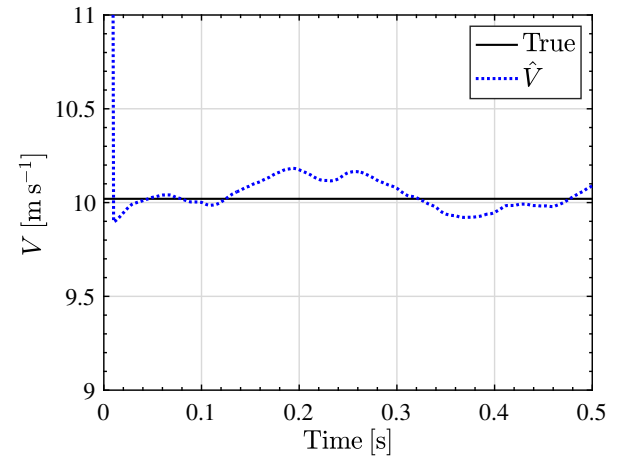
(a) α .(b) V .

Fig. 12. Wind-tunnel test results of airflow vector estimation.

ters were based on NASA's GL-10 [12]. The pitching moment was assumed to be controlled by the tail, and aerodynamic forces on the fuselage and wing were considered in this simulation.

A pre-experiment was conducted to improve the accuracy of the GL-10 simulator, as shown in Fig. 14. Fig. 14(a) shows the picture of the 3D printed GL-10 model. The lift and drag on the fuselage were measured using the small wind tunnel shown in Fig. 14(b). The measured forces were divided by the product of q and the wetted area of the fuselage to obtain C_L and C_D , respectively. The results of the pre-experiments are shown in Fig. 14(c).

The simulation results are shown in Fig. 15; X_e and Z_e denote earth-fixed coordinates; V was set to 30 m s^{-1} , α was set to 10 deg, and σ was set to 40 deg in the initial state. The airspeed along the X_e -axis was increased 5 m s^{-1} stepwise at $t = 5 \text{ s}$. The proposed method changed σ at $t = 5.5 \text{ s}$ to follow the target path. However, the conventional method did not change σ and could not obtain sufficient F_{bx} to stay in the target path, as shown in Fig. 15(a). These results show that aerodynamic force control using airflow vector estimation is indispensable for tilt-wing flights.

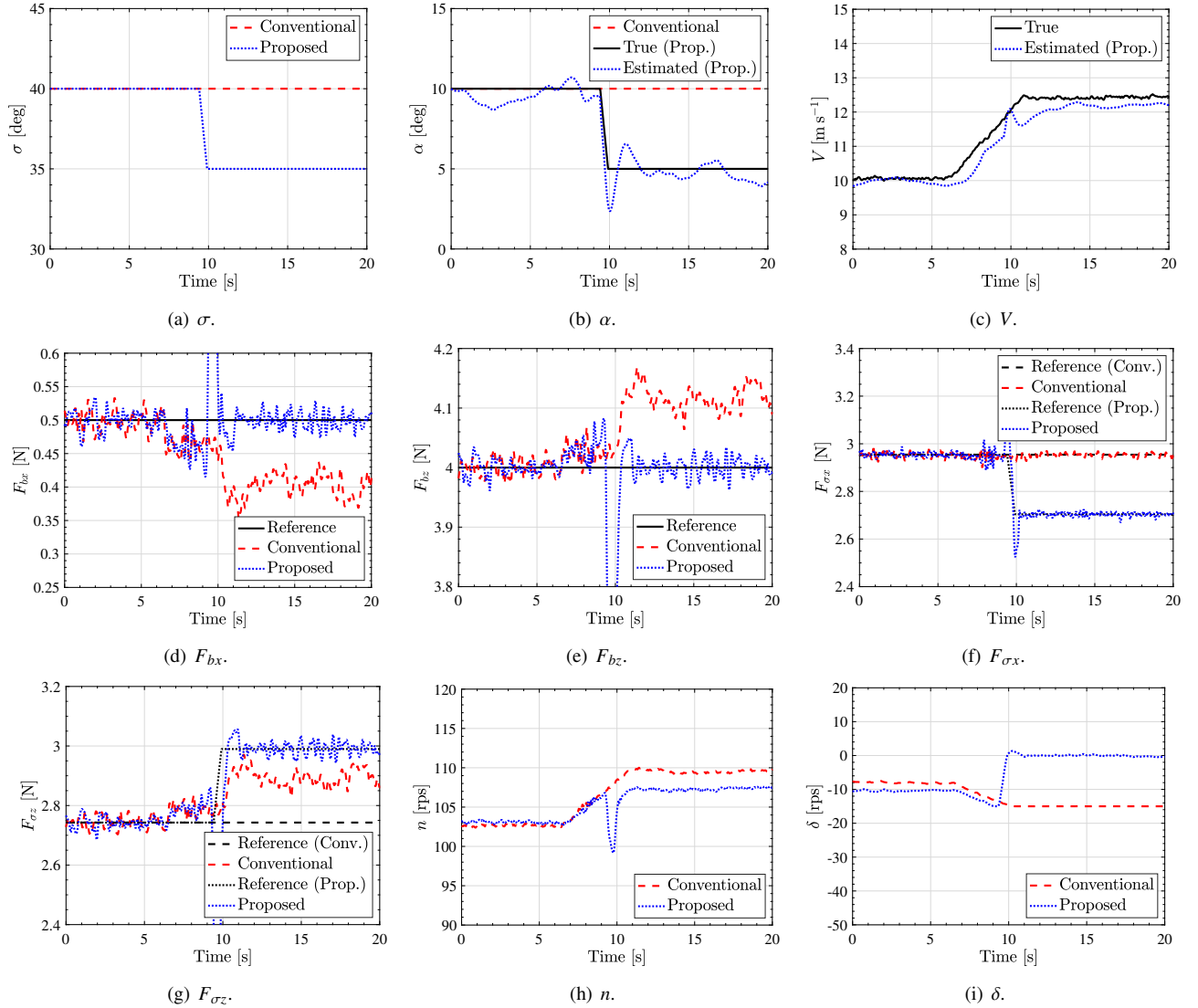


Fig. 13. Wind tunnel test results of aerodynamic force control.

VI. CONCLUSIONS

Remarkably, eVTOL aircraft are attracting considerable attention for secure, efficient, and eco-friendly aviation. In particular, tilt-wing is known to be an efficient configuration. Tilt-wing aircraft tend to be unstable during the transition from hover to cruise. In this study, a new aerodynamic force control of a propeller wing for stability improvement is proposed. The difficulty in the force control of the tilt-wing is that the lift and thrust have limitations that vary with the airflow and tilt angle. Therefore, the proposed method uses airflow vector estimation to monitor the limitations and change the tilt angle to achieve the desired force. The effectiveness of the proposed method was verified experimentally and through simulations.

ACKNOWLEDGMENT

The authors would like to thank Mr. H. Kobayashi from the Japan Aerospace Exploration Agency for his valuable advice and technical assistance with the experiments.

REFERENCES

- [1] Y. Hori, "Future Vehicle Driven by Electricity and Control—Research on Four-Wheel-Motored "UOT Electric March II",," *IEEE Transactions on Industrial Electronics*, vol. 51, no. 5, pp. 954–962, Oct 2004.
- [2] N. K. Borer, M. D. Patterson, J. K. Viken, M. D. Moore, J. Bevirt, A. M. Stoll, and A. R. Gibson, "Design and Performance of the NASA SCEPTOR Distributed Electric Propulsion Flight Demonstrator," in *16th AIAA Aviation Technology, Integration, and Operations Conference*. AIAA, Jun 2016, pp. 1–20.
- [3] N. Adachi, H. Kobayashi, H. Hakoijima, and A. Nishizawa, "An Experimental Study on Energy Regeneration Using Propellers," JAXA, Tech. Rep., 2015, (in Japanese).
- [4] K. Takahashi, H. Fujimoto, Y. Hori, H. Kobayashi, and A. Nishizawa, "Modeling of propeller electric airplane and thrust control using advantage of electric motor," in *2014 IEEE 13th International Workshop on Advanced Motion Control (AMC)*, no. 1. IEEE, Mar 2014, pp. 482–487.
- [5] N. Konishi, H. Fujimoto, Y. Watanabe, K. Suzuki, H. Kobayashi, and A. Nishizawa, "Lift control of electric airplanes by using propeller slipstream for safe landing," in *2015 IEEE International Conference on Mechatronics (ICM)*. IEEE, Mar 2015, pp. 335–340.
- [6] N. Konishi, H. Fujimoto, H. Kobayashi, and A. Nishizawa, "Range extension control system for electric airplane with multiple motors by optimization of thrust distribution considering propellers efficiency," in *IECON 2014 - 40th Annual Conference of the IEEE Industrial Electronics Society*. IEEE, Oct 2014, pp. 2847–2852.

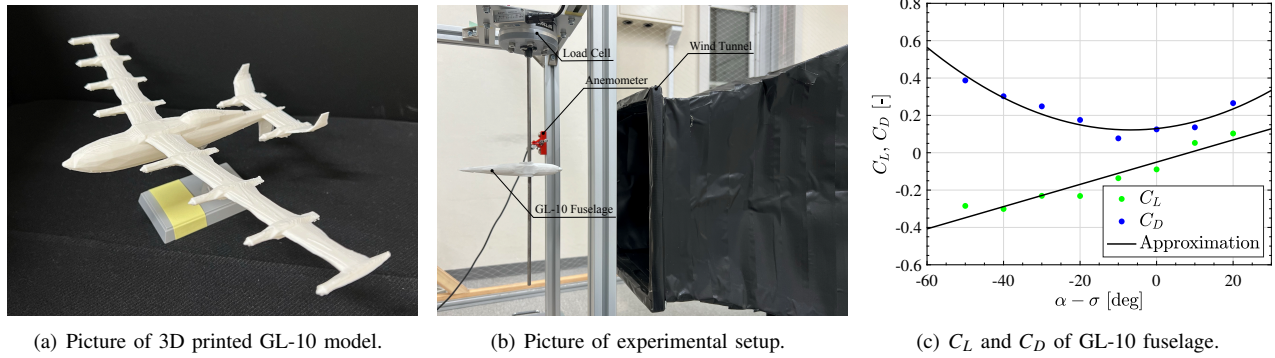


Fig. 14. Pre-experiment for GL-10 simulator.

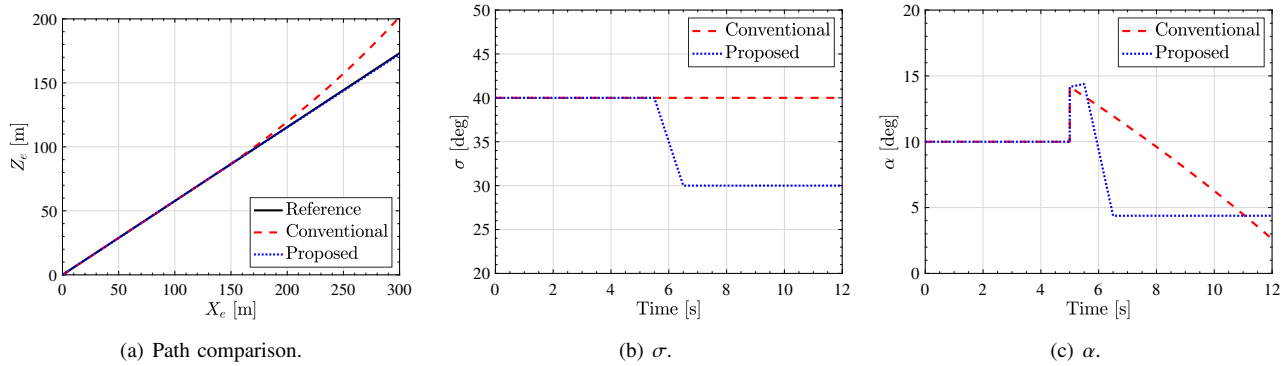


Fig. 15. Simulation flight results of conventional and proposed methods.

- [7] H. Fujimoto and H. Sumiya, "Advanced safety range extension control system for electric vehicle with front- and rear-active steering and left- and right-force distribution," in *2012 IEEE/ASME International Conference on Advanced Intelligent Mechatronics (AIM)*. IEEE, Jul 2012, pp. 532–537.
- [8] W. Johnson, C. Silva, and E. Solis, "Concept Vehicles for VTOL Air Taxi Operations," in *AHS International Technical Meeting on Aeromechanics Design for Transformative Vertical Flight*, Jan 2018.
- [9] K. Muraoka, N. Okada, and D. Kubo, "Quad Tilt Wing VTOL UAV: Aerodynamic Characteristics and Prototype Flight," in *AIAA Infotech@Aerospace Conference*. Reston, Virginia: American Institute of Aeronautics and Astronautics, Apr 2009.
- [10] P. M. Rothhaar, P. C. Murphy, B. J. Bacon, I. M. Gregory, J. A. Grauer, R. C. Busan, and M. A. Croom, "NASA Langley Distributed Propulsion VTOL TiltWing Aircraft Testing, Modeling, Simulation, Control, and Flight Test Development," in *14th AIAA Aviation Technology, Integration, and Operations Conference*. Reston, Virginia: American Institute of Aeronautics and Astronautics, Jun 2014.
- [11] W. J. Fredericks, R. G. McSwain, B. F. Beaton, D. W. Klassman, and C. R. Theodore, "Greased Lightning (GL-10) Flight Testing Campaign," NASA, Tech. Rep., 2017.
- [12] R. G. McSwain, L. J. Glaab, and C. R. Theodore, "Greased Lightning (GL-10) Performance Flight Research—Flight Data Report," NASA, Tech. Rep., Nov 2017.
- [13] R. C. Busan, P. C. Murphy, D. B. Hatke, and B. M. Simmons, "Wind Tunnel Testing Techniques for a Tandem Tilt-Wing, Distributed Electric Propulsion VTOL Aircraft," in *AIAA Scitech 2021 Forum*. Reston, Virginia: American Institute of Aeronautics and Astronautics, Jan 2021, pp. 1–23.
- [14] M. Sato and K. Muraoka, "Flight Controller Design and Demonstration of Quad-Tilt-Wing Unmanned Aerial Vehicle," *Journal of Guidance, Control, and Dynamics*, vol. 38, no. 6, pp. 1071–1082, Jun 2015.
- [15] P. Hartmann, C. Meyer, and D. Moormann, "Unified Velocity Control and Flight State Transition of Unmanned Tilt-Wing Aircraft," *Journal of Guidance, Control, and Dynamics*, vol. 40, no. 6, pp. 1348–1359, Jun 2017.
- [16] L. SANKARALINGAM and C. RAMPRASADH, "A comprehensive survey on the methods of angle of attack measurement and estimation in UAVs," *Chinese Journal of Aeronautics*, vol. 33, no. 3, pp. 749–770, Mar 2020.
- [17] P. Tian and H. Chao, "Model Aided Estimation of Angle of Attack, Sideslip Angle, and 3D Wind without Flow Angle Measurements," in *2018 AIAA Guidance, Navigation, and Control Conference*. Reston, Virginia: American Institute of Aeronautics and Astronautics, Jan 2018.
- [18] M. Oosterom and R. Babuska, "Virtual Sensor for the Angle-of-Attack Signal in Small Commercial Aircraft," in *2006 IEEE International Conference on Fuzzy Systems*. IEEE, 2006, pp. 1396–1403.
- [19] P. Lichota and M. Lasek, "Maximum Likelihood Estimation: A method for flight dynamics - Angle of attack estimation," in *Proceedings of the 14th International Carpathian Control Conference (ICCC)*. IEEE, May 2013, pp. 218–221.
- [20] T. A. Johansen, A. Cristofaro, K. Sorensen, J. M. Hansen, and T. I. Fossen, "On estimation of wind velocity, angle-of-attack and sideslip angle of small UAVs using standard sensors," in *2015 International Conference on Unmanned Aircraft Systems (ICUAS)*. IEEE, Jun 2015, pp. 510–519.
- [21] A. Wenz, T. A. Johansen, and A. Cristofaro, "Combining model-free and model-based angle of attack estimation for small fixed-wing UAVs using a standard sensor suite," in *2016 International Conference on Unmanned Aircraft Systems (ICUAS)*. IEEE, Jun 2016, pp. 624–632.
- [22] P. Simplício, M. Pavel, E. van Kampen, and Q. Chu, "An acceleration measurements-based approach for helicopter nonlinear flight control using Incremental Nonlinear Dynamic Inversion," *Control Engineering Practice*, vol. 21, no. 8, pp. 1065–1077, Aug 2013.
- [23] B. W. McCormick, *Aerodynamics of V/STOL Flight*. Dover Pubns, 1967.
- [24] K. Yokota, H. Fujimoto, and H. Kobayashi, "Observer-based Angle of Attack Estimation for Tilt-Wing eVTOL Aircraft," in *2021 IEEE International Conference on Mechatronics (ICM)*. IEEE, Mar 2021, pp. 1–6.
- [25] H. Kobayahi, A. Nishizawa, and T. Iijima, "Airspeed estimation by electric propulsion system parameters," in *55th Aircraft Symposium*. JSASS, Nov 2017, (in Japanese).
- [26] K. Yokota and H. Fujimoto, "Pitch angle control by regenerative air brake for electric aircraft," *IEEJ Journal of Industry Applications*, vol. 11, pp. 308–316, Mar 2022.

- [27] K. Ohnishi, M. Shibata, and T. Murakami, "Motion control for advanced mechatronics," *IEEE/ASME Transactions on Mechatronics*, vol. 1, no. 1, pp. 56–67, Mar 1996.
- [28] S. Yamada and H. Fujimoto, "Minimum-Variance Load-Side External Torque Estimation Robust Against Modeling and Measurement Errors," *IEEE Journal of Industry Applications*, vol. 9, no. 2, pp. 117–124, Mar 2020.
- [29] R. P. Benedict, *Fundamentals of Temperature, Pressure, and Flow Measurements*. Wiley-Interscience, 1984.
- [30] S. S. Chauhan and J. R. R. A. Martins, "Tilt-Wing eVTOL Takeoff Trajectory Optimization," *Journal of Aircraft*, vol. 57, no. 1, pp. 93–112, Jan 2020.



Kentaro Yokota received his B.E. degree from the Department of Electrical and Electronic Engineering at the University of Tokyo. He is currently working towards his M.S. degree at the Department of Advanced Energy, Graduate School of Frontier Sciences, the University of Tokyo. His research interests include electric aircraft control. He is a student member of the Institute of Electrical Engineers of Japan, the Japan Society for Aeronautical and Space Sciences, the Institute of Electrical and Electronics Engineers, and the American Institute of Aeronautics

and Astronautics.



Hiroshi Fujimoto received his Ph.D. degree in the Department of Electrical Engineering from the University of Tokyo in 2001. In 2001, he joined the Department of Electrical Engineering, Nagaoka University of Technology, Niigata, Japan as a research associate. From 2002 to 2003, he was a visiting scholar at the School of Mechanical Engineering at Purdue University, U.S.A. In 2004, he joined the Department of Electrical and Computer Engineering, Yokohama National University, Yokohama, Japan, as a lecturer, and became an associate professor in

2005. He moved to the University of Tokyo as an Associate Professor in 2010 and became a Professor in 2021. He received the Best Paper Awards from the IEEE Transactions on Industrial Electronics in 2001 and 2013, the Isao Takahashi Power Electronics Award in 2010, the Best Author Prize of SICE in 2010, the Nagamori Grand Award in 2016, and the First Prize Paper Award for IEEE Transactions on Power Electronics in 2016. His research interests include control engineering, motion control, nanoscale servo systems, electric vehicle control, motor drives, visual servos, and wireless motors. He is a senior member of the IEE of Japan and IEEE. He is also a member of the Society of Instrument and Control Engineers, Robotics Society of Japan, and Society of Automotive Engineers of Japan. He was an associate editor of IEEE/ASME Transactions on Mechatronics from 2010 to 2014, IEEE Industrial Electronics Magazine from 2006, IEE of Japan Transactions on Industrial Application from 2013, and Transactions on SICE from 2013 to 2016. He was a chairperson of JSAE vehicle electrification committee from 2014 to 2020 and a chairperson of IEEE/IES Technical Committee on Motion Control from 2012 to 2013.